Supporting Information

Detection of a coherent excitonic state in the layered semiconductor BiI_3

Valentina Gosetti,[†,‡,⊥] Jorge Cervantes-Villanueva,[¶] Davide Sangalli,[§] Alejandro Molina-Sánchez,[¶] Vadim F. Agekyan,[‖] Claudio Giannetti,[†,⊥] Luigi Sangaletti,[†,⊥] Selene Mor,[†,⊥] and Stefania Pagliara[*,†,⊥]

†*Department of Mathematics and Physics, Università Cattolica, I-25133 Brescia, Italy*

‡*Department of Materials Engineering, KU Leuven, Kasteelpark Arenberg 44, 3001 Leuven, Belgium*

¶*Institute of Materials Science (ICMUV), University of Valencia, Catedrático Beltrán 2, E-46980, Valencia, Spain*

§*Istituto di Struttura della Materia-CNR (ISM-CNR), Area della Ricerca di Roma 1, Monterotondo Scalo, Italy*

‖*St. Petersburg State University, St. Petersburg, 199034, Russia*

⊥*Interdisciplinary Laboratories for Advanced Materials Physics (I-LAMP), Università Cattolica, I-25133 Brescia, Italy*

E-mail: stefania.pagliara@unicatt.it

Experimental results

Crystal growth

The single crystal of BiI_3 was grown following the subsequent two-step procedure. Firstly, a crystalline BiI_3 powder is synthesized from a mixture of chemically pure bismuth and iodine powders (weight ratio 2:1). The synthesis is carried out at a temperature of about 200°C in a glass ampoule, the vacuum is 10^{-4} mm Hg. Secondly, the crystalline BiI_3 powder is placed in an evacuated ampoule with a vacuum of 10^{-4} mm Hg. The ampoule is inserted into the furnace, where the powder is slowly (within an hour) heated up to 300°C. Then, a temperature gradient is created along the ampoule, and BiI_3 crystal plates grow in the cold part of the ampoule for one hour. The crystal axis is oriented perpendicular to the plane of the plates.

Equilibrium reflectance measurement

To characterize BiI_3, a PerkinElmer Lambda 950 spectrometer is used to collect the equilibrium reflectance spectrum of BiI_3 at room temperature as shown in Fig 2 (b) in the main text. The spectrum exhibits a sharp resonance at 2 eV [1] ascribed to the lowest-energy exciton, and a broader feature centered at 2.48 eV due to the L-U-M transitions in the Brillouin zone. [2]

Optical set-up

Temporal chirp of the white-light supercontinuum

A schematic picture of the setup for the transient reflectance collection is inserted in Fig. S1. The first building block of our experimental set-up is the femtosecond pulsed laser LIGHT CONVERSION PHAROS, which delivers 280-fs-long pulses with a 1030 nm central emission wavelength and 37.5 μJ/pulse energy per pulse. By means of an optical pulse picker,

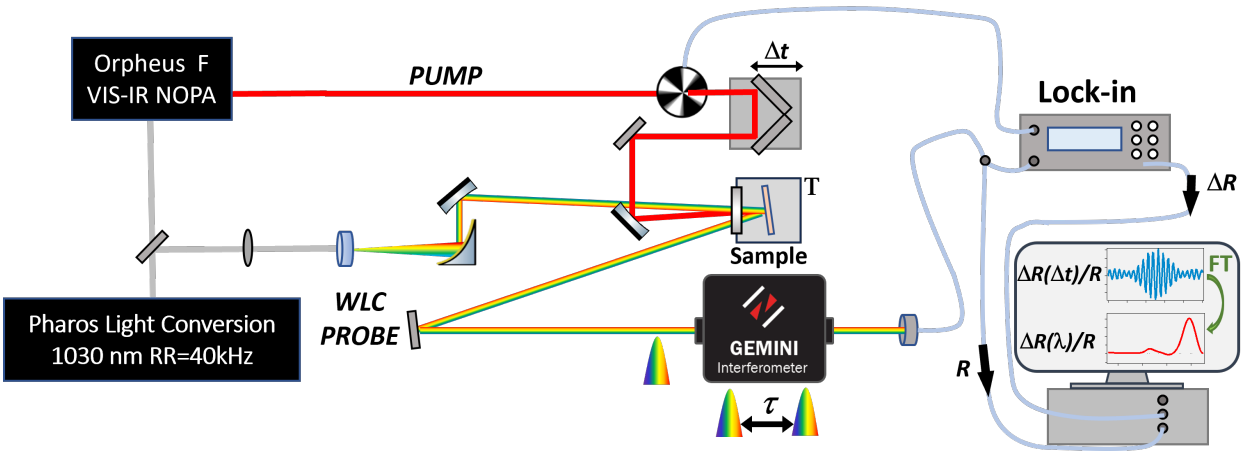

Figure S1: Scheme of the optical set-up exploited for the acquisition both of the transient and the equilibrium reflectance.

PHAROS has a tunable repetition rate (Rep. Rate) up to 400 kHz. A 20/80 beam splitter divided the PHAROS output into two beams. 30 μJ/pulse of the PHAROS emission is used to pump the non-collinear optical parametric amplifier (NOPA) ORPHEUS-F, which generates an output spanning from 640 nm to 900 nm. The beam is, then, compressed by a double prism compressor. As a pump, we used the 650 nm output of the ORPHEUS-F with a spectral bandwidth of $\Delta\lambda = 12nm$. The remaining 7.5 μJ/pulse are used for the probe line. The energy per pulse is reduced to 1.5 μJ/pulse with a quarter wave plate and a polarizer. The outcoming beam is focused on a 4-mm-thick YAG (Yttrium Alluminium Garnet) crystal to generate a supercontinuum (WLG). With the bandpass filter, Thorlabs FSH0950 the 500 nm-950 nm region of the white light is selected to exclude the fundamental excitation. A motorized line delay stage is used to control the pump-probe delay changing the length of the optical path of the pump. The acquisition is made with a GEMINI interferometer by NIREOS. To collect the reflectance we used a Si-based photodiode (PD). The acquired signal is split into two-component: a lock-in amplified signal that filters out the pump-probe correlated signal (ΔR) modulated at the frequency of the pump beam chopper and a DC signal that is the non-correlated reflectance component of the sample. The two collected interferograms are Fourier transformed and the transient reflectance $\frac{\Delta R}{R_0}$ is acquired. The sample is inserted in a closed-cycle helium cryostat that allows performing transient opti-

cal measurements at low temperatures down to 17K. The sample was cleaved in situ. The measurement was carried out at 50K, at low ambient pressure, with a Rep. Rate of 40 kHz and a fluence of 50 $\frac{\mu J}{cm^2}$. The instrumental response function, defined as the cross-correlation between the pump and the probe measured at the sample position, is limited by the temporal duration of the pump pulse and results in 70 fs.

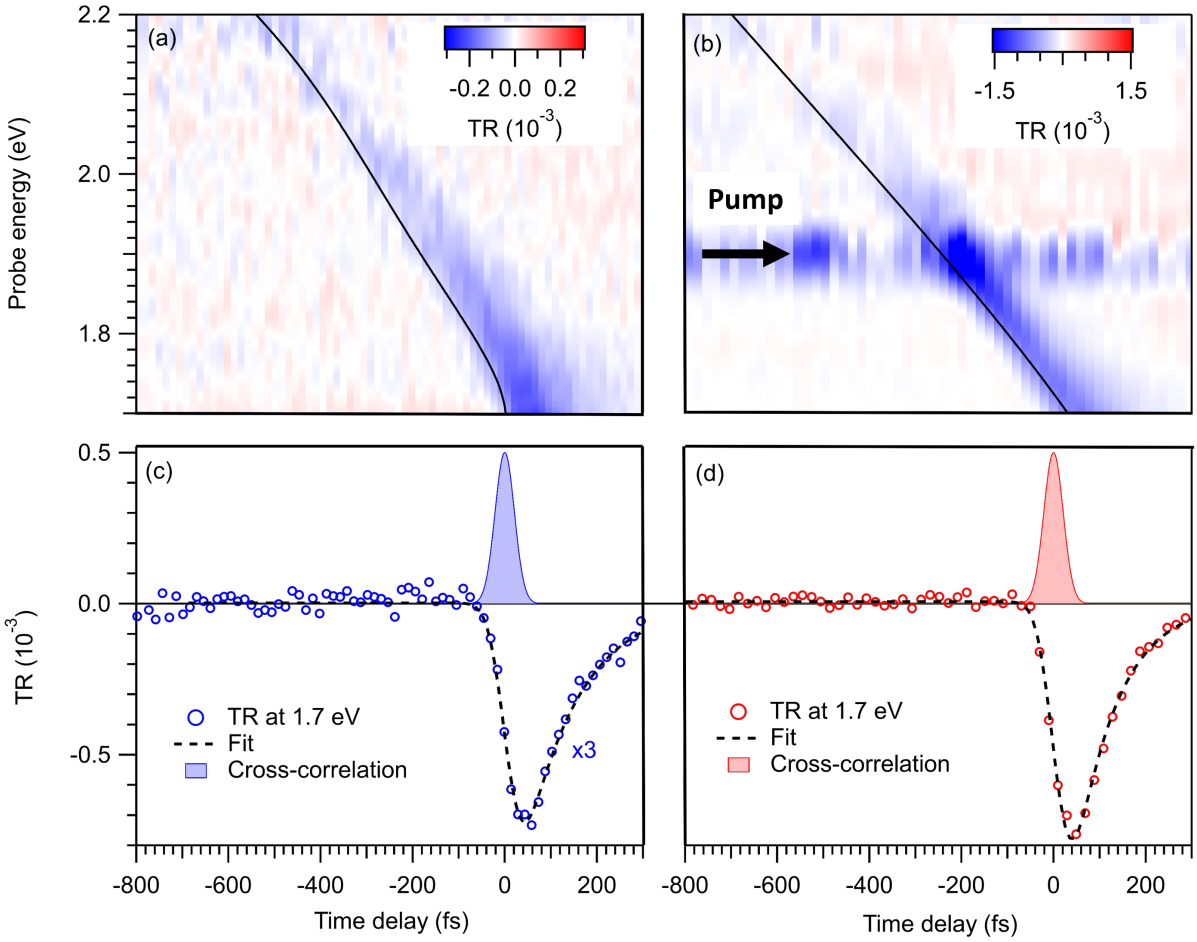

Figure S2: Transient reflectance of HOPG as a function of probe energy left axis and delay time bottom axis collected with a photon energy of 2.79 eV (a) and 1.91 eV (b). The solid black curves are the time zeros dispersion. Horizontal linecuts at 1.7 eV with the relative fit are inserted in (c) and (d) for the non-resonant and resonant pumping conditions, respectively. The blue and red shades feature are the resuting punm-probe cross-correlation.

To collect the transient reflectance of BiI_3 as a function of pump-probe delay and probe wavelength, a continuum white light probe in the 1.9 eV-2.3 eV range was exploited. The use of a broad probe wavelength window induces a temporal chirp of a few hundred fs in

the response of BiI_3. To study the probe-wavelength-dependent response, the dispersion of the chirp has to be taken into account in the analysis. To evaluate the temporal chirp, the transient reflectance of highly-oriented pyrolitic graphite (HOPG) was collected as a function of pump-probe delay time and probe wavelength with a 2.79-eV- and 1.9-eV-pump photon energy, Fig. S2 (a) and (b) respectively. The HOPG sample was located inside a closed-cycle helium cryostat at low pressure and room temperature. The HOPG is used due to its instantaneous response and its fast relaxation dynamic, shorter than the set-up resolution. Therefore, HOPG is useful to evaluate the pump-probe correlation time and the dispersion of the time zero in the probed energy region. To evaluate these quantities, horizontal line cuts were extracted from the map. The horizontal linecuts at 1.7 eV for the two colormaps are inserted as blue and red markers courves in Fig. S2 (c) and (d) respectively. To fit the transient reflectance evolution with the pump-probe time delay, we used a convolution between a Gaussian function, that takes into account the pump-probe-cross-correlation, and a response function, which is a Heaviside function located at the pump-probe overlap time multiplied by a fast exponential decaying function. As a result, the cross-correlation between the pump and the probe is (70 ± 10) fs, and the temporal chirp is the black line shown in Fig. S2. The resulting fitting curves are inseted as black dashed lines in Fig. S2 (c) and (d) and the cross-correlation intensity profiles are the shaded blue and red features. The chirp is determined by the experimental set-up and the white light generation (WLG), therefore the extrapolated time-zeros-dispersion is the same also for BiI_3. The time zero of BiI_3 transient reflectance was aligned according to the extrapolated temporal chirp.

BiI_3 equilibrium reflectance at low temperature

White-light supercontinuum pulses between 1.55 eV and 2.48 eV have been exploited to record the equilibrium reflectance of a single crystal of BiI_3. The white light is generated by a 4-mm-thick YAG (Yttrium Alluminium Garnet) crystal. The generated light is collimated with a parabolic mirror. A single crystal BiI_3 sample was mounted on a Cu sample holder

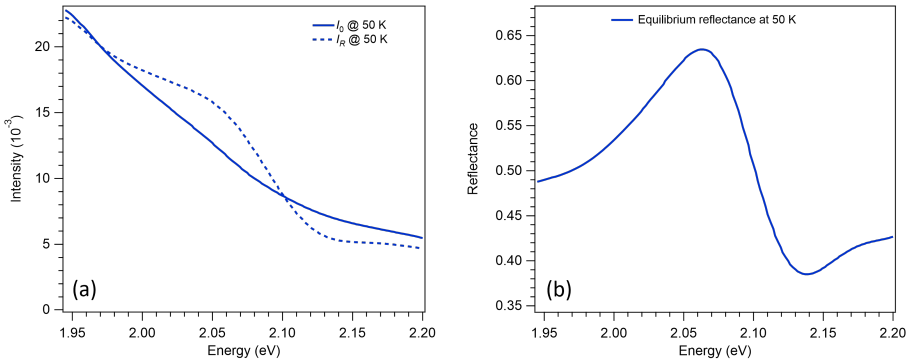

Figure S3: (a) The acquired intensity of the supercontinuum I_0 (solid blue line) and the reflected light I_R by BiI_3 at 50 K (dashed blue line) (b) Reflectance spectrum of BiI_3 at 50 K.

inside a helium closed-cycle cryostat to control the temperature. To collect the reflected intensity (I_R) we used a GEMINI interferometer by NIREOS. The reflected intensity is collected with a Si-based photodiode and the DC signal is acquired by a lock-in. Then to have the energy-dependent reflectance the acquired output is Fourier transformed. A sketch of the set-up is inserted in Fig. S1. The set-up is the same one used for the acquisition of the transient reflectance. The pump beam is blocked after the ORPHEUS-F output by a beam blocker. An example of the reflected intensity is the dashed blue line in Fig. S3 (a). As a reference, the spectrum of the non-interacting supercontinuum (I_0, for instance, the solid blue line in figure Fig. S3 (a)) was collected. The final reflectance R is, then, the ratio between the reflected light and the incident light ($R = \frac{I_R}{I_0}$). The collected reflectance at 50 K is shown in Fig. S3 (b).

Data analysis procedure

The first step of the analysis consists of finding the right parametrization of the BiI_3 equilibrium reflectance R_{eq}. A Tauc-Lorentz model has been chosen to reproduce R_{eq}. As part of this model, the complex dielectric function is described by:

$$\tilde{\epsilon}_{TL} = \epsilon_{r,TL} + i \cdot \epsilon_{i,TL} = \epsilon_{r,TL} + i \cdot (\epsilon_{i,T} \times \epsilon_{i,L}) \tag{1}$$

The Tauc term in the imaginary dielectric function ($\epsilon_{i,T}$) represents the response of the direct gap material caused by the inter-band transition, while the excitonic resonances are described by lorentian oscillators ($\epsilon_{i,L}$). In our case, three Tauc-Lorentz oscillators have been exploited to reproduce the excitonic resonances. The complete imaginary part of the dielectric function is:

$$\epsilon_{i,TL} = \epsilon_{i,T} \times \epsilon_{i,L} = \begin{cases} \sum_{i=1}^{3} \frac{1}{E} \frac{A_i E_{0i} \Gamma_i (e - E_g)^2}{(E^2 - E_{0i}^2)^2 + \Gamma_i^2 E^2} & \text{if } E > E_g \\ 0 & \text{if } E \leq E_g \end{cases} \tag{2}$$

where A_i, Γ_i, and E_{0i} are the amplitude, the full-width-half-maximum (FWHM), and the center of the i-th oscillator, respectively. The real part of the dielectic function is retrived by the Kramer-Kroenig integration:

$$\epsilon_{TL,r}(E) = \epsilon_r(\infty) + \frac{2}{\pi} P \int_{E_g}^{\infty} \frac{\xi \cdot \epsilon_{TL,i}(\xi)}{\xi^2 - E^2} d\xi \tag{3}$$

where P is the Cauchy principal value. For the Tauc-Lorentz model the real part of the dielectric function ($\epsilon_{TL,i}$) is the one reported by Jellison and Modine in 1996.[3] The reflectance is then defined as:

$$R = \frac{(n-1)^2 + k^2}{(n+1)^2 + k^2} \tag{4}$$

where n and k are the real and imaginary part of the complex refractive index $\tilde{n} = n + ik$. These are related with the dielectric function as:

$$n = \{\frac{1}{2}[(\epsilon_1^2 + \epsilon_2^2)^{\frac{1}{2}} + \epsilon_1]\}^{\frac{1}{2}} \tag{5}$$

$$k = \{\frac{1}{2}[(\epsilon_1^2 + \epsilon_2^2)^{\frac{1}{2}} - \epsilon_1]\}^{\frac{1}{2}} \tag{6}$$

Thereby, the reflectance at 50 K has been fitted using the Tauc-Lorentz procedure. The acquired and fitted reflectance are shown in Fig. 1 (b) of the main text. We report the

reproduced R_{eq} in Fig. S4 as a dashed black line to show more in details the parametrization results. The first Tauc-Lorentz oscillator, located at (2.06 ± 0.01) eV (orange-shaded peak) with a FWHM of (40 ± 5) meV, is assigned to the first bright exciton, while the second at (2.17 ± 0.01) eV and with a linewidth of (60 ± 5) meV is ascribed to the second bright exciton (green-shaded peak), according to absorption measurement on BiI_3 thin film.[4] We note that the total linewidth of the first excitonic resonance includes also the experimental resolution of 37 meV. The deconvoluted linewidth of the first exciton is (15 ± 5) meV. Moreover, the third oscillator located at (2.31 ± 0.01) eV (violet-shaded peak) has a broader width of (240 ± 5) meV and represents a collection of the higher-order excitons, that in our analysis represents a background since it is outside our probed energy window (highlighted on the top of Fig. S4). The found Tauc energy gap is (1.97 ± 0.01) eV and it is the same for all the oscillators.

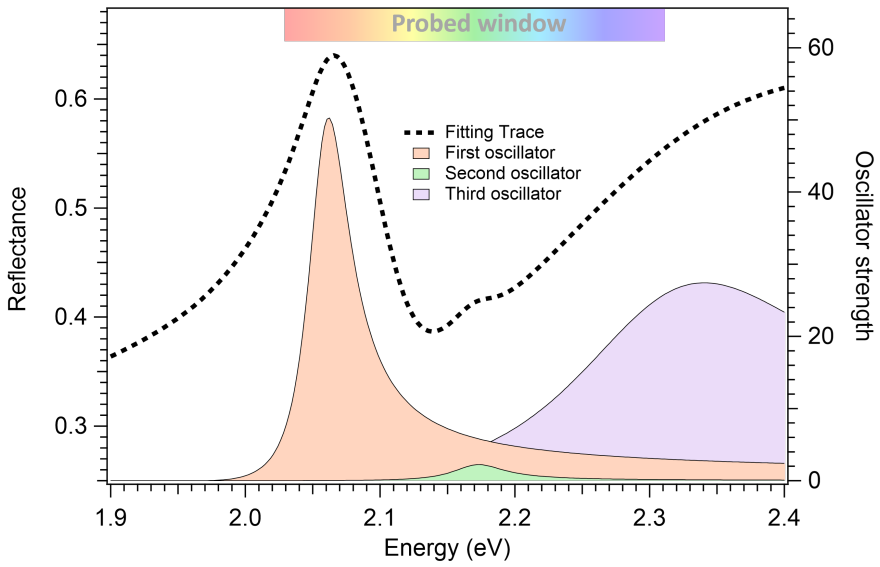

Figure S4: Reproduced equilibrium reflectance (black dashed line), where the three excitonic oscillators are underlined by the orange, green and violet peaks.

The second step of the analysis procedure comprises the modelization of the out-of-equilibrium reflectance (R_{neq}). To reproduce it, we consider a shift in the energy position (ΔE_i), a change in the linewidth ($\Delta \Gamma_i$), a variation of the peak intensity (ΔA_i) for each oscillator, and a modification in the Tauc energy gap (ΔE_g). The resulting imaginary part of the dielectric function is:

$$\epsilon_{i,TL,neq} = \begin{cases} \sum_{i=1}^{3} \frac{1}{E} \frac{(A_i + \Delta A_i)(E_{0i} + \Delta E_i)(\Gamma_i + \Delta\Gamma_i)(E - E_g - \Delta E_g)^2}{(E^2 - (E_{0i} + \Delta E_i)^2)^2 + (\Gamma_i + \Delta\Gamma_i)^2 E^2} & \text{if } E > E_g + \Delta E_g \\ 0 & \text{if } E \leq E_g + \Delta E_g \end{cases} \tag{7}$$

The out-of-equilibrium reflectance (R_{neq}) is then calculated following the procedure illustrated above.

Adding up all the elements, the energy-dependent transient reflectance spectra of BiI_3 were fitted using the following function:

$$\Delta R = \frac{R_{neq} - R_{eq}}{R_{eq}} \tag{8}$$

where R_{eq} is the parametrized equilibrium reflectance and R_{neq} is the out-of-equilibrium reflectance

Thereby, the fitting function (ΔR) is used to interpolate the energy-dependent transient reflectance (TR) traces acquired at selected time delays. A representative fit is shown in Fig. 2 (b) and (e) of the main text, for the quasi- and out-of-resonance pumping, respectively. In this analysis, the third exciton, being a background, is kept fixed for all the time delays. In addition, due to the suppression of photoinduced free carriers ruled by the quasi-resonant pumping, the Tauc energy gap is also fixed in all the delays. Conversely, the Tauc energy gap is left free to change due to the free-carrier-induced band gap renormalization in the out-of-resonant pumping. The transient evolution of both intensity and energy of the first exciton oscillator with quasi-resonant pumping as a return of the fit are shown in Fig. 4 and discussed in the main text. To clarify the analysis described in the main text, the time-resolved dynamics of these two quantities were evaluated with a global fit through the sum of three terms, assigned in the main text as coherent excitons, incoherent excitons, and coherent vibrations. The whole response function is convoluted with a gaussian function with FWHM of 70 fs that represents the experimental resolution. Firstly, the coherent exciton

signal rises within the pump-pulse cross-correlation duration and has a single-component decay evolution. Secondly, the incoherent exciton population is described by a single rise time followed by a double exponential decay function. Lastly, the coherent vibrations are periodic modulations described by a damped cosine function, with damped time longer than the probed temporal window.

Theoretical calculations

Computational details

The theoretical analysis of the equilibrium and non-equilibrium optical properties of BiI_3 is based on first-principles calculations. The calculation of the electronic structure is performed within the framework of density functional theory (DFT), using the Quantum ESPRESSO package[5–7] and the Perdew-Burke-Ernzerhof (PBE) exchange-correlation functional.[8] The van der Waals interaction is considered according to the Tkatchencko-Scheffler model (TS-vdW).[9] Due to the heaviness of the constituent atoms and the resulting strong spin-orbit interaction, fully relativistic norm-conserving pseudopotentials are used from PseudoDojo,[10] including Bi $5d$ and I $5d$ semi-core states.[11,12] Experimental lattice parameters are used in this work with a = 7.52 Å and c = 20.7 Å.[13] All the DFT calculations are performed with a plane-wave cutoff of 80 Ry and a **k**-grid of 8x8x8, following the Monkhorst-Pack method.[14] The GW and GW+BSE calculations for the quasiparticle corrections and the equilibrium and non-equilibrium optical properties are carried out in Yambo code.[15–17] The quasiparticle corrections are obtained at the G_0W_0 level, using the plasmon-pole approximation. The dielectric matrix is computed considering 300 bands and using a terminator for the electronic Green's function G.[18] The calculation of the optical properties considering excitonic effects is performed on top of the GW results. Equilibrium optical properties are computed solving the Bethe-Salpeter equation within the Tamm-Dancoff approximation,[19] while non-equilibrium optical properties are calculated through the evolution of the equation of motion for the time-dependent density matrix $\rho(t)$ under the effects of a pump field.[20] To compute the static kernel of the BSE, 200 bands are considered, while 10 valence bands and 4 conduction bands are used for the calculation of the excitonic transitions. In the non-equilibrium case, both the pump and the probe fields are computed with a time step of 10 as. We use a two step integrator (Runge-Kutta 2^{nd} order), where however each single step is based on an inversion operation instead of the simple Euler approach. The inverstion step is the adaptation to

the density matrix case of the algorithm present in,[21] eq. 24. Both fields are modelled by a QSSIN function so that the phase can be controlled. In particular, the pump field has a time duration of 180 fs with an in-plane polarization and an intensity of 2x10^6 $\frac{kW}{cm^2}$. On the other side, the probe field arrives 25 fs after the maximum of the pump pulse and has a time duration of 95 fs with an in-plane polarization perpendicular to that of the pump and an intensity of 10^2 $\frac{kW}{cm^2}$.

Analysis of the role of the detuning in the quasi-resonant case

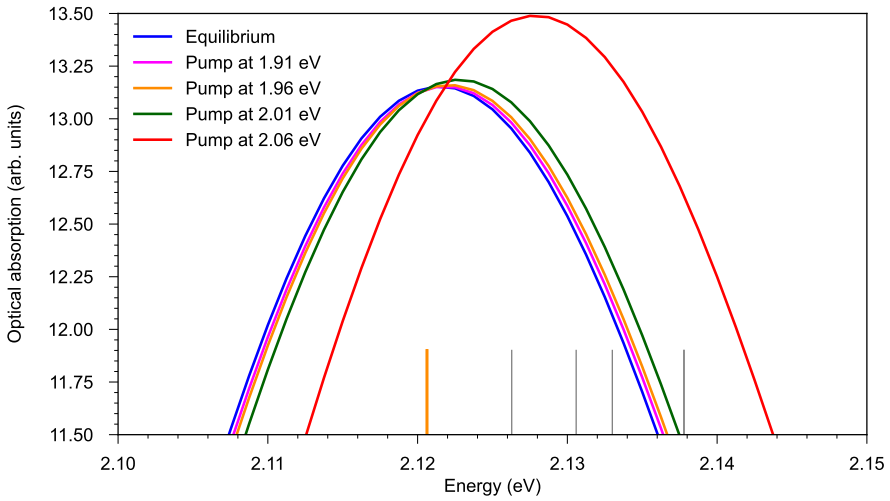

Figure S5: Behaviour of the first bright exciton according to the pump energy. The yellow bar represents the bright exciton while the gray bars represent the dark ones.

Experimentally, the first bright exciton is found to be at 2.06 eV. To study the quasi-resonant case, a pump at 1.91 eV is used, resulting in a detuning of 150 meV. The same detuning is used in the numerical simulations (bright peak at 2.12 eV, pump pulse at 1.97 eV). Since we are not formally in resonance, we here show the behaviour of the excitonic peak as a function of the detuning. To this end, we plot in Fig. S5 the behaviour of the excitonic peak for different pump energies and different detuning paramters, 1.91 eV (detuning 210 meV), 1.96 eV (detuning 160 meV), 2.01 eV (detuning 110 meV), 2.06 eV (detuning 60 meV). We keep the pump fluence constant. We also performed simulations at zero detuning.

However in such case the very strong absorption leads to a drastic change in the spectrum and we do not show it here. Comparing the different spectra we observe that there is no qualitative difference in the shape of the spectra, just an increase in the intensity of the excitonic peak due to higher exciton population as the detuning is reduced. This confirms that the signal computed at 150 detuning is not a specific feature of the very low exciton population, but that it is stable against the changes in the pump freqeuncy. As a side effect the large detuning ensures a presence of a rather low density of coherent excitons, and thus that we stay below the exciton Mott transition.

Analysis of the time dependence of the signal on the relative phase of pump and probe

Quasi-resonant case

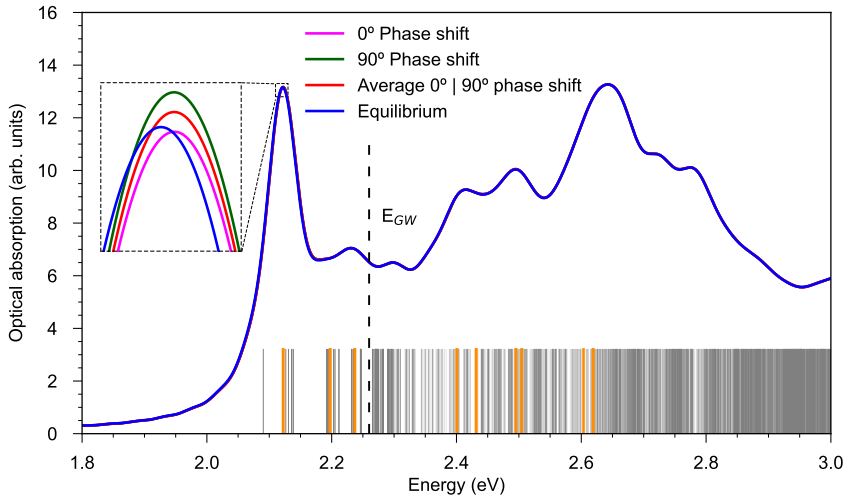

Figure S6: Optical absorption spectra of BiI_3 at equilibrium and when pumping at 1.97 eV for different probe phases. The dashed black line is the direct gap energy. The yellow bars represent the bright excitons and the gray bars the dark excitons.

To generate a quasi-resonant excitation we pump at 1.97 eV. The resulting absorption spectra as well as the equilibrium spectrum are depicted in Fig. S6. We observe that depend-

ing on the phase shift of the probe with respect to the pump, the change of the excitonic peak is different. Indeed the signal is very sensitive to the relative phase of the pump and the probe, resulting in time dependent oscillations as a function of the pump-probe delay (Dynamical Franz Keldysh effect). From an experimental point of view, these oscillations cannot be measured since (i) they are very fast, and (ii) it is necessary a control of the phase of the probe, e.g. to work with phase-locked pulses. Instead the experiment is performed without controlling the relative phase, and moreover averaging over many measurements with random phases. This washes out the above discussed oscillations. Thus, in order to be able to compare the theoretical results with the experimental measurements, we mimic the averaging procedure by summing the signal obtained with two opposite relative phases at fixed delay: 0^{o} and 90^{o}.

Non-resonant case

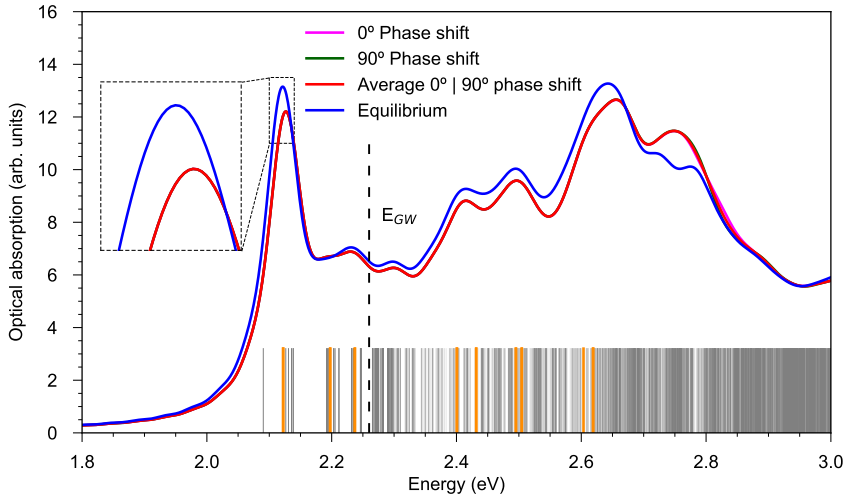

Figure S7: Optical absorption spectra of BiI_3 at equilibrium and when pumping at 2.79 eV for different probe phases. The dashed black line is the direct gap energy. The bright excitons are represented by yellow bars, and the dark excitons by gray bars.

For the non-resonant case we pump in the continuum with a pump energy of 2.79 eV, as shown in Fig. S7. We perform the above discussed averaging procedure also in this case.

However, in contrast to what it is observed for the quasi-resonant excitation, here the non-equilibrium spectrum is not affected by the phase shift of the probe with respect to the pump. This is likely due to the fact that we pump in the continuum and many frequencies are present, so that the Dynamical Franz Keldysh effect is washed out.

References

(1) Kaifu, Y. Excitons in layered BiI3 single crystals. *Journal of Luminescence* **1988**, *42*, 61–81.

(2) Jellison, G. E.; Ramey, J. O.; Boatner, L. A. Optical functions of BiI_3 as measured by generalized ellipsometry. *Phys. Rev. B* **1999**, *59*, 9718–9721.

(3) Jellison, J., G. E.; Modine, F. A. Parameterization of the optical functions of amorphous materials in the interband region. *Applied Physics Letters* **1996**, *69*, 371–373.

(4) Yasunami, T.; Nakamura, M.; Inagaki, S.; Toyoda, S.; Ogawa, N.; Tokura, Y.; Kawasaki, M. Molecular beam epitaxy of two-dimensional semiconductor BiI3 films exhibiting sharp exciton absorption. *Applied Physics Letters* **2021**, *119*, 243101.

(5) Giannozzi, P. et al. QUANTUM ESPRESSO: a modular and open-source software project for quantum simulations of materials. *Journal of Physics: Condensed Matter* **2009**, *21*, 395502.

(6) Giannozzi, P. et al. Advanced capabilities for materials modelling with QUANTUM ESPRESSO. *Journal of Physics: Condensed Matter* **2017**, *29*, 465901.

(7) Giannozzi, P.; Baseggio, O.; Bonfà, P.; Brunato, D.; Car, R.; Carnimeo, I.; Cavazzoni, C.; de Gironcoli, S.; Delugas, P.; Ferrari Ruffino, F.; Ferretti, A.; Marzari, N.; Timrov, I.; Urru, A.; Baroni, S. QUANTUM ESPRESSO toward the exascale. *The Journal of Chemical Physics* **2020**, *152*, 154105.

(8) Perdew, J. P.; Burke, K.; Ernzerhof, M. Generalized Gradient Approximation Made Simple. *Phys. Rev. Lett.* **1996**, *77*, 3865–3868.

(9) Tkatchenko, A.; Scheffler, M. Accurate Molecular Van Der Waals Interactions from Ground-State Electron Density and Free-Atom Reference Data. *Phys. Rev. Lett.* **2009**, *102*, 073005.

(10) van Setten, M.; Giantomassi, M.; Bousquet, E.; Verstraete, M.; Hamann, D.; Gonze, X.; Rignanese, G.-M. The PSEUDODOJO: Training and grading a 85 element optimized norm-conserving pseudopotential table. *Computer Physics Communications* **2018**, *226*, 39–54.

(11) Scherpelz, P.; Govoni, M.; Hamada, I.; Galli, G. Implementation and Validation of Fully Relativistic GW Calculations: Spin–Orbit Coupling in Molecules, Nanocrystals, and Solids. *Journal of Chemical Theory and Computation* **2016**, *12*, 3523–3544.

(12) Giustino, F. *Materials Modelling Using Density Functional Theory: Properties and Predictions*; Oxford University Press, 2014.

(13) Nason, D.; Keller, L. The growth and crystallography of bismuth tri-iodide crystals grown by vapor transport. *Journal of Crystal Growth* **1995**, *156*, 221–226.

(14) Monkhorst, H. J.; Pack, J. D. Special points for Brillouin-zone integrations. *Phys. Rev. B* **1976**, *13*, 5188–5192.

(15) Marini, A.; Hogan, C.; Grüning, M.; Varsano, D. yambo: An ab initio tool for excited state calculations. *Computer Physics Communications* **2009**, *180*, 1392–1403.

(16) Sangalli, D. et al. Many-body perturbation theory calculations using the yambo code. *Journal of Physics: Condensed Matter* **2019**, *31*, 325902.

(17) Marsili, M.; Molina-Sánchez, A.; Palummo, M.; Sangalli, D.; Marini, A. Spinorial formulation of the *GW*-BSE equations and spin properties of excitons in two-dimensional transition metal dichalcogenides. *Phys. Rev. B* **2021**, *103*, 155152.

(18) Bruneval, F.; Gonze, X. Accurate *GW* self-energies in a plane-wave basis using only a few empty states: Towards large systems. *Phys. Rev. B* **2008**, *78*, 085125.

(19) Strinati, G. Application of the Green's functions method to the study of the optical properties of semiconductors. *La Rivista del Nuovo Cimento (1978-1999)* **1988**, *11*, 1–86.

(20) Sangalli, D. Excitons and carriers in transient absorption and time-resolved ARPES spectroscopy: An ab initio approach. *Phys. Rev. Mater.* **2021**, *5*, 083803.

(21) Attaccalite, C.; Grüning, M. Nonlinear optics from an ab initio approach by means of the dynamical Berry phase: Application to second- and third-harmonic generation in semiconductors. *Phys. Rev. B* **2013**, *88*, 235113.